Suspending a Solid Sphere in Laminar Inertial Liquid Flow—Experiments and Simulations

Junyuan Mo, Zhengming Gao, and Yuyun Bao
State Key Laboratory of Chemical Resource Engineering, School of Chemical Engineering, Beijing University of Chemical Technology, Beijing 100029, China

Zhipeng Li
State Key Laboratory of Chemical Resource Engineering, School of Chemical Engineering, Beijing University of Chemical Technology, Beijing 100029, China

School of Engineering, University of Aberdeen, Aberdeen AB24 3UE, U.K

J. J. Derksen
School of Engineering, University of Aberdeen, Aberdeen AB24 3UE, U.K

Chemical Engineering, Delft University of Technology 2628 BLDelft, Netherlands

DOI 10.1002/aic.14756
Published online February 25, 2015 in Wiley Online Library (wileyonlinelibrary.com)

The critical conditions for the suspension of single, spherical solid particles by a liquid flow in a square container driven by a rotating disk have been determined. In the experiments, the motion of the sphere has been visualized quantitatively. The conditions are such that the flow in the container is laminar (Reynolds numbers based on the rotating disk characteristics are in the range 10–40). The Archimedes numbers of the spheres are of order 1. The suspension process has also been numerically simulated with full resolution of the liquid flow, including the flow around the sphere, and the translational and rotational motion of the sphere. The simulations recover the critical conditions to within 3% in terms of the rotational speed of the disk. Also the sphere's trajectory in the container is reproduced well by the simulations. © 2015 American Institute of Chemical Engineers *AIChE J*, 61: 1455–1469, 2015
Keywords: solid suspension, rotating disk, quantitative visualization, direct numerical simulation, lattice–Boltzmann method, stirred tank

Introduction

Suspending solid particles in a liquid flow is relevant in many situations and applications. Examples are slurry pipelines, sediment transport in rivers and coastal regions, and heterogeneous and catalytic chemical reactors. In batch reactors, suspension of particles is a means of promoting solid-liquid mass transfer by exposing as much as possible solid surface area to a strong turbulent flow that is usually generated by an impeller. Designing effective ways of creating flow conditions that achieve entrainment of solids, therefore, contributes to process performance and efficiency. In the research on this topic, emphasis has been placed—for good reason—on finding critical conditions for solids suspension: what minimum flow, and thus what minimum power input, is needed to mobilize and suspend solid particles? In this field, seminal work has been performed by Zwietering[1] who systematically addressed the above question for the flow generated by impellers in mixing tanks. Zwietering's work has been extended and refined by many others (Nienow,[2] Baldi et al.,[3] and Davies[4]). Montante et al.[5] combined experimental and computational (computational fluid dynamics, CFD) methods to study solids suspension in mixing tanks. Recent work on solids suspension in stirred tanks deals with mixtures of different types of particles[6,7] and addresses important questions about the interaction between the different particle types.

Besides reactor engineering, the topic of incipient motion of solids in liquids has attracted considerable attention by environmental fluid mechanists who study sediment transport.[8,9] Recent work has reviewed and highlighted the limited reproducibility of past experiments on incipient motion and suggests ways to improve this.[10]

Conceptually, the situation of entraining solid particles in a liquid flow is rather simple. A collection of solid particles has settled on the bottom of a container that contains mostly liquid. Agitation of the liquid creates a flow that exerts forces on the particles. If the flow gets sufficiently strong, particles start moving, first rolling over the bottom or over one another, later being entrained by the liquid and moving through the container. The drag force is the major coupling between solid and liquid. With this realization, some of the complications become apparent. We are dealing with drag in the vicinity of a wall and/or in the vicinity of many other

Correspondence concerning this article should be addressed to Z. Li at lizp@mail.buct.edu.cn.

© 2015 American Institute of Chemical Engineers

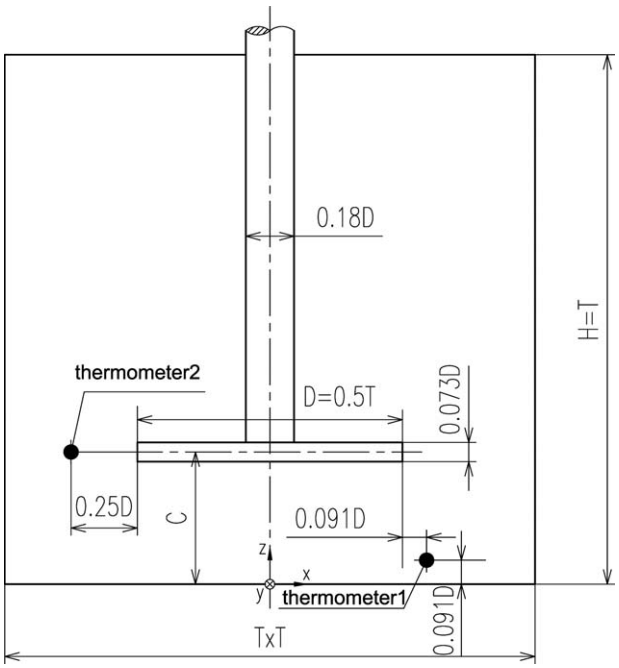

Figure 1. Agitated tank geometry: a circular disk spins in a square tank with side length $T = 0.220$ m.

The off-bottom clearance of the disk is either $C = 0.25$ or $0.20T$. The origin of the coordinate system is in the center of the bottom. Temperatures were measured before and after each flow experiment at the locations indicated.

particles. For the former situation, drag near a wall, theoretical results for drag due to simple (shear) flow on single spherical particles in the low (particle-based) Reynolds number range are available;[11–13] some computational studies[14–16] have extended this to higher Reynolds numbers. Segre and Silberberg reported lateral migration effects of particles moving in the vicinity of a wall.[17] Also knowledge on the drag force on spherical particles in dense, homogeneous suspensions is ubiquitous.[18] Complications relate in the first place to the very inhomogeneous distribution of solids closely above the bottom. If a bed of solids has formed, the solids volume fraction can vary by orders of magnitude from within the bed to slightly above the bed over distances of a few particle diameters. For such inhomogeneous distributions, drag force relations are not available. In the second place, the flow that entrains the particles might not be a simple, canonical flow. It might, for instance, be a turbulent boundary layer that additionally is perturbed by the presence of the particles.

Recent experimental and computational work steps back from some of the complications as outlined above and considers the fundamental aspects of solids suspension mechanisms in relatively simple situations under well-controlled conditions.[19,20] A similar approach is taken in this article where we follow in great detail the scenario for entrainment of a single spherical particle by the laminar (though inertial) liquid flow in a container generated by a spinning disk. Different from other works, our experimental configuration resembles an agitated tank and in follow-up research, we plan to systematically add complexity (an impeller as used in practical applications instead of a disk, multiple particles, higher Reynolds numbers, and eventually turbulence). The current setup allows for detailed and accurate quantitative visualization of the motion of the spherical particle. In addition, the mobilization scenarios are designed such that they can be simulated directly, "directly" meaning with full resolution of the flow and the interactions between solid and liquid.

Therefore, the aims of the research described in this article are (1) to provide a highly reproducible base-case of solids suspension in an agitated tank, the results of which can be used to derive and tune models and (CFD) simulation tools; (2) identify—by relating experimental and simulation results—solids suspension mechanisms in agitated, confined flows; (3) critically validate our own computational approach by comparison with the detailed experiments; (4) to build on this base-case and systematically work toward more complex agitated systems and suspension mechanisms.

The organization of this article is as follows: in the next section, the experimental flow system is described including identification of the dimensionless numbers that govern the flow. Subsequently, experimental methods for determining critical entrainment conditions and quantitative visualization of sphere motion are presented. Then, our existing numerical framework is outlined briefly where emphasis is placed on the necessity of modeling the lubrication force between particle and bottom wall. In the "Results and Discussion" section, first experimental observations are given, followed by the comparison of experimental and computational results. The computations give detailed insights in the flow in the direct vicinity of the sphere which allows the experimental results to be placed in context. The final section summarizes the main conclusions and suggests future research directions.

Experimental Setup

Flow system

Flow is being generated by spinning a circular disk in a square, flat bottomed container filled with a Newtonian liquid. This geometry, including a coordinate system that will be used throughout the article, is shown in Figure 1. Gravity points in the negative z-direction. The main dimension of the tank is the length of its base: $T = 0.220$ m. The other dimensions of tank and disk have been derived from T, as indicated in the figure. Once the geometry is fixed, the flow in the tank is fully characterized by a Reynolds number that we define as $Re = \frac{ND^2}{\nu}$ with $D = T/2$ the disk diameter, N the rotational speed of the disk (in rev/s), and ν the kinematic viscosity of the liquid. The Reynolds number in this study is of the order of 10 so that the flow is laminar, however, with appreciable inertial effects.

At the top of the tank, the liquid has a free surface. The bottom and side walls are transparent for optical access. The liquid is a silicone oil (purchased from Shanghai Lubao Company, density $\rho = 977$ kg/m^3) which was chosen for its weak dependency of viscosity on temperature. Preliminary experiments were done with glycerol. Glycerol's pronounced temperature-dependent viscosity in combination with viscous heating was, however, detrimental for reproducibility of the experiments. This instigated the choice for a silicone oil. Directly before and after each experiment, the temperature of the oil was measured at two locations, as indicated in Figure 1. The viscosity assigned to the specific experiment (and used to, e.g., determine the Reynolds number) is based on the average of the four temperature readings and the relationship between temperature and viscosity as measured with

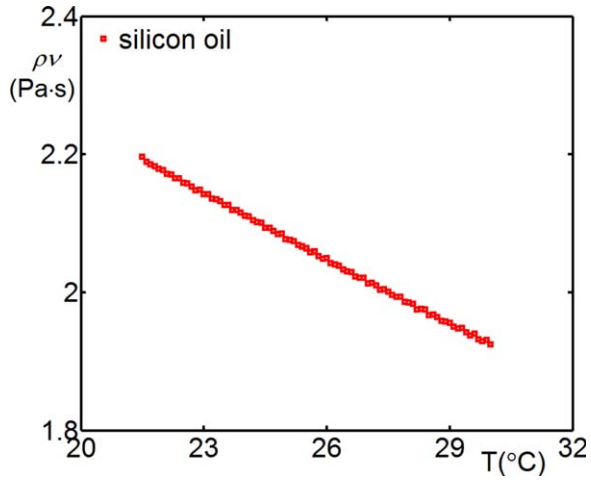

Figure 2. Measured dynamic viscosity as a function of temperature of the silicone oil used in the experiments.

[Color figure can be viewed in the online issue, which is available at wileyonlinelibrary.com.]

a RS150L Rheometer (Haake, Germany), see Figure 2. Temperature gradients do develop in the experiment. However, the maximum difference between the four measured temperatures was less than 0.5°C, which implies a variability of less than 1% in the viscosity. During whole of the experimental campaign, the room temperature was controlled at 23°C.

Various spherical solid particles with different diameters d_p and densities ρ_p were used in the experiments (Table 1). The particles were carefully selected for their spherical shape and the tolerance in the diameter (as measured in different directions) is within 1%. The presence of a spherical particle in the flow gives rise to additional dimensionless numbers. Various choices can be made in this respect. In this article, we will be working with the density ratio ρ_p/ρ, the ratio of particle diameter over disk diameter d_p/D, the Archimedes number $Ar \equiv \frac{g d_p^3}{\nu^2}\frac{\Delta\rho}{\rho}$ (with g gravitational acceleration, and $\Delta\rho \equiv \rho_p - \rho$), and an inertial Shields number[21] defined as $\theta \equiv \frac{\rho N^2 D^2}{g\Delta\rho d_p}$. The Archimedes number relates to a Reynolds number of the particle settling in quiescent liquid. The inertial Shields number is indicative for the ratio of inertial stress exerted on the particle by the flow due to the rotating disk and gravity-induced stress.

Experimental procedure and visualization

An important goal of the experiments is to quantify critical conditions for the sphere getting suspended. As a metric, we determine the lowest rotational speed of the disk for which the sphere is lifted off the bottom of the tank. For this, the experimental procedure is as follows: the sphere is placed in still liquid on the bottom of the tank with center location $(x, y, z) = (0.0, -0.409T, 0.5d_p)$. The disk is set to rotate and accelerates very slowly (by 2 rpm/min). The flow this generates makes the sphere roll over the bottom to the center of the tank. At some point, the sphere starts rising along a vertical line that coincides approximately with the center line of the tank. The sphere eventually hits the bottom surface of the disk, rolls underneath the disk and eventually is ejected into the bulk of the tank. The critical rotational speed of the disk at lift off of the sphere we call N_{LO}. The procedure for determining N_{LO} is repeated at least two times. The value of N_{LO} is reproducible within 1.5%. The reported values for N_{LO} (see the Results section) are averages of duplicate experiments. Lift-off disk speeds as a function of particle properties (size and density) and the disk's off-bottom clearance C (Figure 1) are important outcomes of this study.

Once lift-off disk speeds have been determined, particle trajectories are measured by means of quantitatively visualizing the motion of the sphere: rolling over the bottom, rising vertically near the center of the tank, and rolling underneath the disk along a spiraling path. The complete and well-defined scenario for measuring solid suspension has been designed so that it can be reproduced in numerical simulations (to be discussed in this article as well). The scenario as executed in the visualization experiments involves a much faster acceleration of the disk (typically by 100 rpm/s) toward the critical rotational speed based on the lift-off experiments as described earlier. If the sphere does not get suspended, the procedure is repeated with the target rotational speed increased by 1 rpm. Surprisingly, critical lift-off rotational speeds N_{LO} as measured with high-acceleration rates hardly differ from those at the lower acceleration rates (by less than 1%) and differences might as well be due to differences in viscosity.

The motion of the sphere is tracked by two high-speed camera's (FASTCAM-ultima APX, Photron Company). As shown in Figure 3, Camera A looks from the side and captures the vertical rise trajectory of the sphere between bottom and disk. Camera B looks up through the bottom and is used to record the trajectory of the initial rolling over the bottom and the spiraling motion underneath the disk. The spheres were painted white, and strong lighting was used to get clear and contrast-rich images. Typical frames taken from below and from the side are presented in Figure 4. The different stages of particle motion were captured in separate experiments and with frame rates and resolutions that depend on estimates of local particle velocity. The horizontal motion over the bottom and the vertical motion toward the disk are relatively slow and were recorded at a rate of 250 frames per second (fps) for the glass and silicon nitride spheres and at 125 fps for the plastic sphere (the latter moves slower) which allowed the maximum camera resolution of 1024 × 1024 pixels^2 to be used. The motion underneath the disk is much faster and is filmed at 1000 fps for the glass and silicon nitride spheres and 250 fps for the plastic sphere with a resolution of 512 × 512 pixels^2. The frame rates for the different stages (and particles) have been selected sufficiently high so that motion blur is virtually absent in the camera frames.

The digital camera frames were processed and analyzed in a Matlab environment to determine the center location of the

Table 1. Experimental Input Parameters

Case	Particle	$\rho_p/\rho(-)$	$C/T(-)$	d_p (mm)	$\nu\rho$ (Pa·s)	Ar (−)
E1	Glass	2.50	0.25	10	2.143	3.07
E2				8	2.137	1.58
E3				5	2.151	0.38
E4			0.2	10	2.149	3.06
E5				8	2.143	1.57
E6				5	2.140	0.39
E7	Silicon nitride	3.33		10	2.148	4.74
E8	Plastic	1.43		10	2.110	0.91

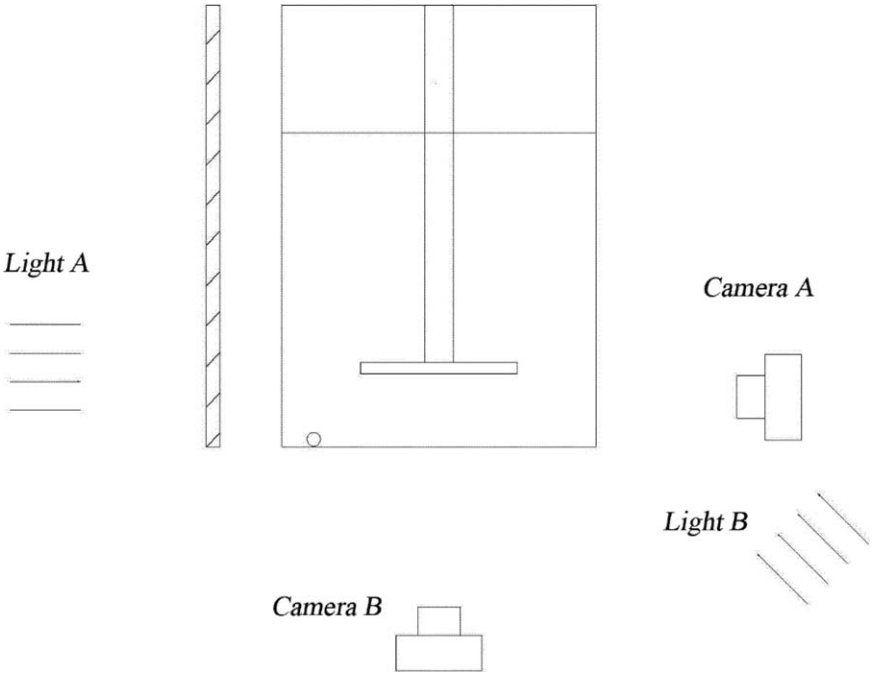

Figure 3. Optical layout: Camera A captures the side view; Camera B the bottom view.

sphere as a function of time. First, the Canny Edge Detector[22] was used as a preprocessing step to identify pixels that are on the circular edge of the image of the sphere in each frame. A Hough transform[23] was selected to group all the edge pixels according to the equation of a circle. The accuracy of the latter step is enhanced by the fact that we know (from a calibration) how many pixels correspond with the sphere radius. The image processing procedure has been illustrated in Figure 5. The center location of the sphere is determined with an uncertainty of 1 pixel. For the bottom-view frames, 1 pixel corresponds to 0.235 mm with the 1024^2 as well as with the 512^2 resolution; for the side view, 1 pixel corresponds to 0.063 mm.

An overview of the input parameters of the (in total eight) experimental cases is given in Table 1. The main input variables in the experiments are the particle (five different solid spheres have been used), and the distance between the bottom of the tank and the bottom surface of the disk (symbol C, see Figure 1) for which two values were considered. With C, we control—to some extent—the strength of the flow over the bottom of the tank.

Numerical approach

The systems as studied experimentally were also investigated numerically. In the numerical simulations, it was attempted to accurately mimic the geometry and physical conditions of the experiment—including the transients associated to the startup of the flow—and to fully resolve the hydrodynamics, including the flow around the sphere and its associated translational and rotational motion.

The lattice–Boltzmann (LB) method[24,25] was used to solve the liquid flow field. More specifically, the scheme proposed by Somers and coworkers[26,27] was applied. It uses a uniform, cubic grid and steps in time in an explicit manner. In the

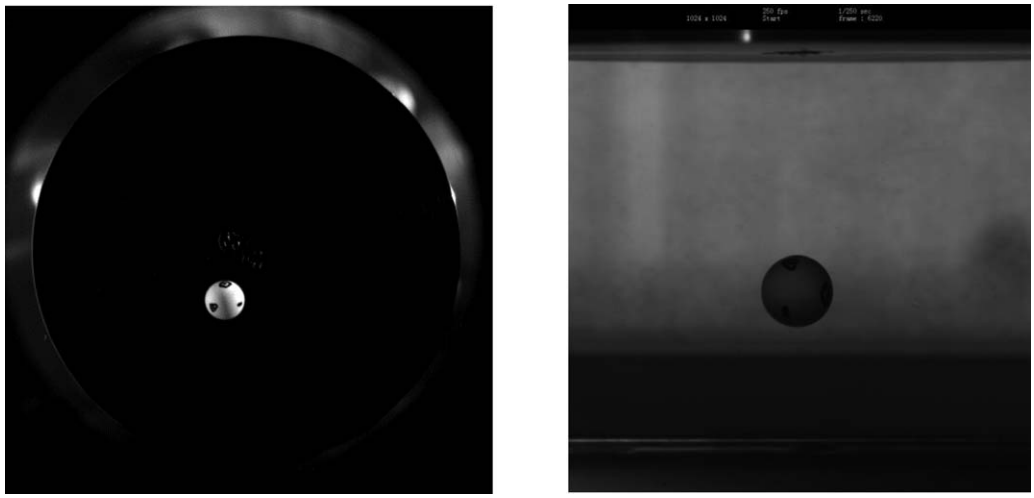

Figure 4. Sample frames.

Left: bottom view with the sphere rolling under the disk; right: side view with the sphere rising toward the disk.

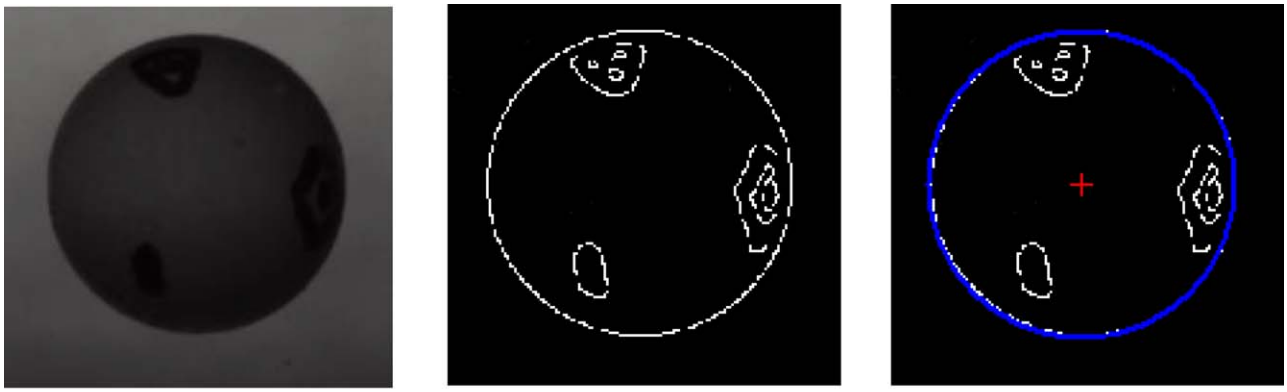

Figure 5. Image processing steps in detection of the sphere position: (a) raw camera frame; (b) image after edge detection; (c) image with fitted circle and center location.

[Color figure can be viewed in the online issue, which is available at wileyonlinelibrary.com.]

simulations, the grid spacing (symbol Δ) and time step (Δt) are the units of space and time, respectively, these are termed "lattice units." The translation to and from physical systems is made by matching the dimensionless numbers in simulations with those in experiments. In general, LB methods use a compressible model for the fluid. As we want to simulate incompressible flow, the fluid's speed $|\mathbf{u}|$ should be kept much lower than the speed of sound. In the LB framework, the speed of sound is of order one in lattice units. Therefore, we require $\mathbf{u}\cdot\mathbf{u} \ll 1$. This criterion is achieved by restricting the tip speed of the disk ($v_{tip}=\pi ND$) to values of order 0.1 in lattice units. The tip speed is a good measure for the highest liquid velocity in the tank. In numerical terms, this restriction means that we use a small time step: we need many time steps (of the order of a few thousand) to complete one disk revolution.

The no-slip walls of the tank (bottom and side walls) are imposed by a halfway bounce-back boundary condition.[25] The free-slip condition at the top surface is implemented by a halfway specular reflection rule.[25] The rotating disk and shaft are represented by a large set of off-grid points on their surface with a spacing of 0.7Δ. At these points, we enforce no-slip by applying a force on the liquid that is controlled in such a way that the liquid velocity at the surface points (determined via linear interpolation from the lattice) matches the solid surface velocity due to the rotation. This variant of the immersed boundary method was developed in 1999[28] and has as been applied to agitated flow systems many times.

The solid sphere is also accounted for by means of the immersed boundary method. The local forces on the liquid to maintain no-slip at the surface of the sphere are integrated over the sphere's surface to determine the total hydrodynamic force and torque on the sphere.[29] In addition to the hydrodynamic force and torque, the sphere feels net gravity (gravity minus buoyancy) and lubrication forces (see below for more details) that are subsequently used to numerically solve the sphere's equations of translational and rotational motion. The updated location and translational and rotational sphere velocities are fed back to the liquid flow as updated no-slip boundary conditions, thus creating a tight and realistic coupling between flow and sphere dynamics.[30] A calibration procedure[29,31,32] has been applied to correctly place the off-grid surface points that represent the sphere in the immersed boundary method.

The sphere collides with the container walls according to a two-parameter model[33] involving a restitution coefficient $e=1$ and a friction coefficient $\mu=0.1$. For solid particles immersed in liquid, the restitution coefficient is not a sensitive parameter as most of the dissipation associated with a collision takes place in the liquid, not on hard-sphere contact.[34] A nonzero friction coefficient μ is needed to allow for rolling over solid surfaces with the precise nonzero value of μ of less importance.[35] The sphere collides with the disk in a manner akin to soft spheres interactions, with a repulsive force being applied when the sphere volume starts to overlap the disk volume. The strength of repulsion is such that for typical sphere-disk encounters the collision time is of the order of $10\Delta t$. Over this time interval, the disk rotates about 1°.

An important modeling aspect of the simulations is the lubrication force between sphere and bottom wall. In the lift-off experiments, the sphere moves over and closely above the bottom for a considerable amount of time. If the width

Table 2. Lift-Off Impeller Speed N_{LO} and Derived Quantities

Case	Particle	$\rho_p/\rho(-)$	$C/T(-)$	d_p (mm)	$v\rho$ (Pa·s)	Ar (−)	N_{LO} (rpm)	$v_{tip,LO}$ (m/s)	Re_{LO} (−)	θ_{LO} (−)
E1	Glass	2.50	0.25	10	2.143	3.07	342	1.97	31.44	2.66
E2				8	2.137	1.58	326	1.88	30.06	3.02
E3				5	2.151	0.38	310	1.79	28.40	4.37
E4			0.2	10	2.149	3.06	284	1.64	26.04	1.83
E5				8	2.143	1.57	274	1.58	25.19	2.13
E6				5	2.140	0.39	263	1.51	24.21	3.14
E7	Silicon nitride	3.34		10	2.148	4.74	410	2.36	37.61	2.46
E8	Plastic	1.43		10	2.110	0.91	120	0.69	11.21	1.14

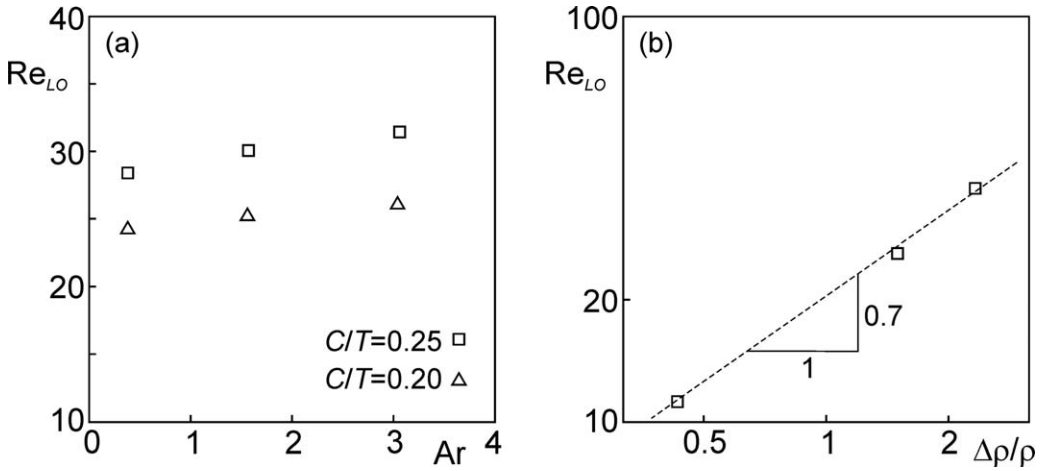

Figure 6. (a) Lift-off Reynolds number as a function of the Archimedes number for glass spheres; off-bottom disk clearance as indicated.

(b) Lift-off Reynolds number of $d_p = 10$ mm spheres of different density for $C/T = 0.2$ (note the double-logarithmic scale in panel [b]).

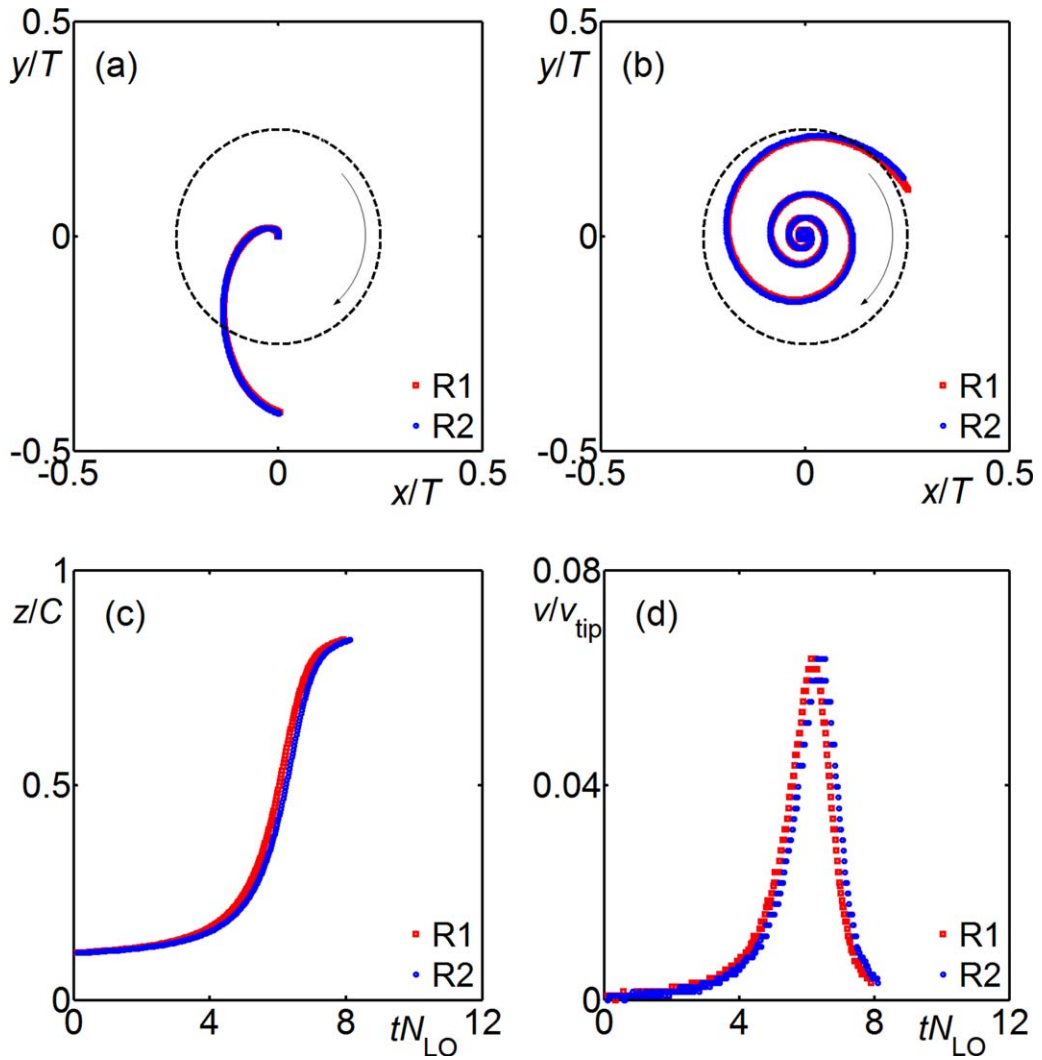

Figure 7. Sphere motion for experimental case E1 (10 mm glass sphere and $C/T = 0.25$).

(a) Rolling motion over the bottom; (b) spiraling motion under the disk; (c) vertical location as a function of time; (d) vertical velocity as a function of time. The panels show two realizations of the experiment (R1 and R2). The direction of rotation of the disk has been indicated in panels (a) and (b). In the bottom panels, $t = 0$ is defined as the moment the gap between bottom wall and sphere is $0.1d_p$. [Color figure can be viewed in the online issue, which is available at wileyonlinelibrary.com.]

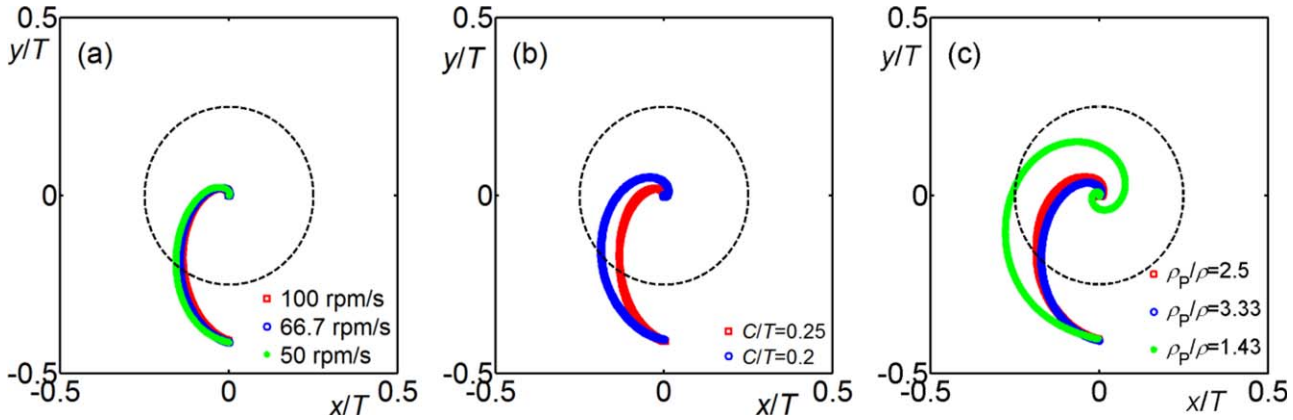

Figure 8. Trajectories of $d_p = 10$ mm spheres over the bottom of the tank.

(a) Effect of disk acceleration at conditions E1 (Table 2); disk accelerations of 100 rpm/s, 66.7 rpm/s, and 50 rpm/s as indicated. (b) Effect of the disk's off-bottom clearance (E1 vs. E4) at 100 rpm/s acceleration. (c) Effect of sphere density at $C/T = 0.20$ at 100 rpm/s acceleration. [Color figure can be viewed in the online issue, which is available at wileyonlinelibrary.com.]

of the gap between the tank bottom and the sphere surface (symbol s) is typically less than one lattice spacing Δ and the sphere has a velocity component in the direction normal to the bottom, the flow simulation does not sufficiently resolve the hydrodynamic interaction between the bottom wall and the sphere. For that reason, we then supplement the hydrodynamic force as obtained from the immersed boundary/LB method with the lubrication force in radial direction (which is the wall-normal direction and thus the vertical direction for bottom-sphere interactions). Analytical expressions for the lubrication force are available based on a creeping flow assumption in the gap between the solid surfaces.[36] To smoothly switch between lubrication forces being active (at small s) and inactive (at larger s), a procedure proposed by Nguyen and Ladd[37] has been followed. It involves the parameter s_0 which is the distance below which the lubrication force becomes active. To avoid divergence of the lubrication force for $s \downarrow 0$ and to account for surface roughness, a second parameter s_1 saturates the lubrication force for small s. The eventual expression for the wall-sphere radial lubrication force reads[21]

$$\begin{aligned}
\mathbf{F_{lub}} &= -\frac{3}{2}\rho\nu d_p^2\left(\frac{1}{s_1}-\frac{1}{s_0}\right)(\mathbf{n}\cdot\mathbf{u_p})\mathbf{n} \quad && s \le s_1 \\
\mathbf{F_{lub}} &= -\frac{3}{2}\rho\nu d_p^2\left(\frac{1}{s}-\frac{1}{s_0}\right)(\mathbf{n}\cdot\mathbf{u_p})\mathbf{n} \quad && s_1 < s < s_0 \\
\mathbf{F_{lub}} &= \mathbf{0} && s \ge s_0
\end{aligned} \tag{1}$$

with $\mathbf{n}$ the unit normal to the wall, pointing into the liquid (e.g., $\mathbf{n}=\mathbf{e_z}$ for the bottom wall), and $\mathbf{u_p}$ the velocity of the sphere. Throughout this study, $s_0 = 0.1 d_p$ and $s_1 = 10^{-4} d_p$. Tangential lubrication forces and torques have been neglected in this study because they are much weaker than the radial lubrication force.[36] We will compare results of simulations that include with those that do not include the lubrication force model.

The overall spatial resolution of the simulations is dictated by the sphere. One needs of the order of 10 lattice distances over a sphere diameter ($d_p \approx 10\Delta$) to properly resolve the flow around it at moderate, sphere-based Reynolds numbers.[29] Therefore (as an example), with a 10 mm sphere, and given the uniform, cubic lattice, the grid size for the entire tank becomes 220-cubed. The impeller then has a diameter of $D \approx 110\Delta$. Given compressibility constraints (disk tip speed not exceeding 0.1 in lattice units), the rotational speed of the disk is approximately $N \approx 3\times10^{-4}/\Delta t$ which implies that the disk makes one revolution in about 3300 time steps. To match a certain experimental Reynolds number (say $Re = \frac{ND^2}{\nu} = 30$), the kinematic viscosity needs to be set to $\nu \approx 0.12$ (in lattice units).

The impact of resolution on the results has been checked by comparing simulations on four different grids (such that $d_p = 8\Delta, 10\Delta, 12\Delta$, and 14Δ, respectively) that have the same dimensionless numbers, and thus represent the same physical situation.

Results

Lift-off impeller speeds

In Table 2, the results of lift-off experiments have been summarized. A first observation is that, for the glass spheres, the lift-off disk speed is to a fair approximation independent of the size of the sphere: reducing the sphere diameter by a factor of 2 (and thus its weight by a factor of 8) reduces the lift-off disk speed by less than 10% (for $C/T = 0.25$ as well as for $C/T = 0.20$). This observation—that has been graphically displayed in Figure 6a—contradicts the hypothesis that the inertial Shields number θ is the controlling parameter for lift off. Such a hypothesis is based on the suspending force scaling with inertial stress times surface area of the sphere $F_{susp} \propto \rho N^2 D^2 d_p^2$, and net gravity being $F_{ng} \propto g\Delta\rho d_p^3$. Their ratio is equal to $\theta \equiv \frac{\rho N^2 D^2}{g\Delta\rho d_p}$. From Table 2, it is clear, however, that θ is not constant at lift off for the same particle material and at fixed C/T. The critical disk speed being almost independent of particle size does suggest that the suspending force scales, just as the sphere's weight, with the volume of the sphere, not with its surface area. Figure 6a also shows—not surprisingly—that placing the disk closer above the tank bottom makes suspending the sphere easier.

The second major observation relates to the lift-off disk speed as a function of the density of the solid material, the sphere is made of (at constant sphere diameter $d_p = 10$ mm and constant $C/T = 0.20$). The hydrodynamic force required to suspend the sphere has to overcome gravity which is proportional to $\Delta\rho$. By plotting $\Delta\rho/\rho$ vs. Re_{LO} (at constant disk diameter and almost constant viscosity the latter is a dimensionless measure for N_{LO}), as done in Figure 6b, it is

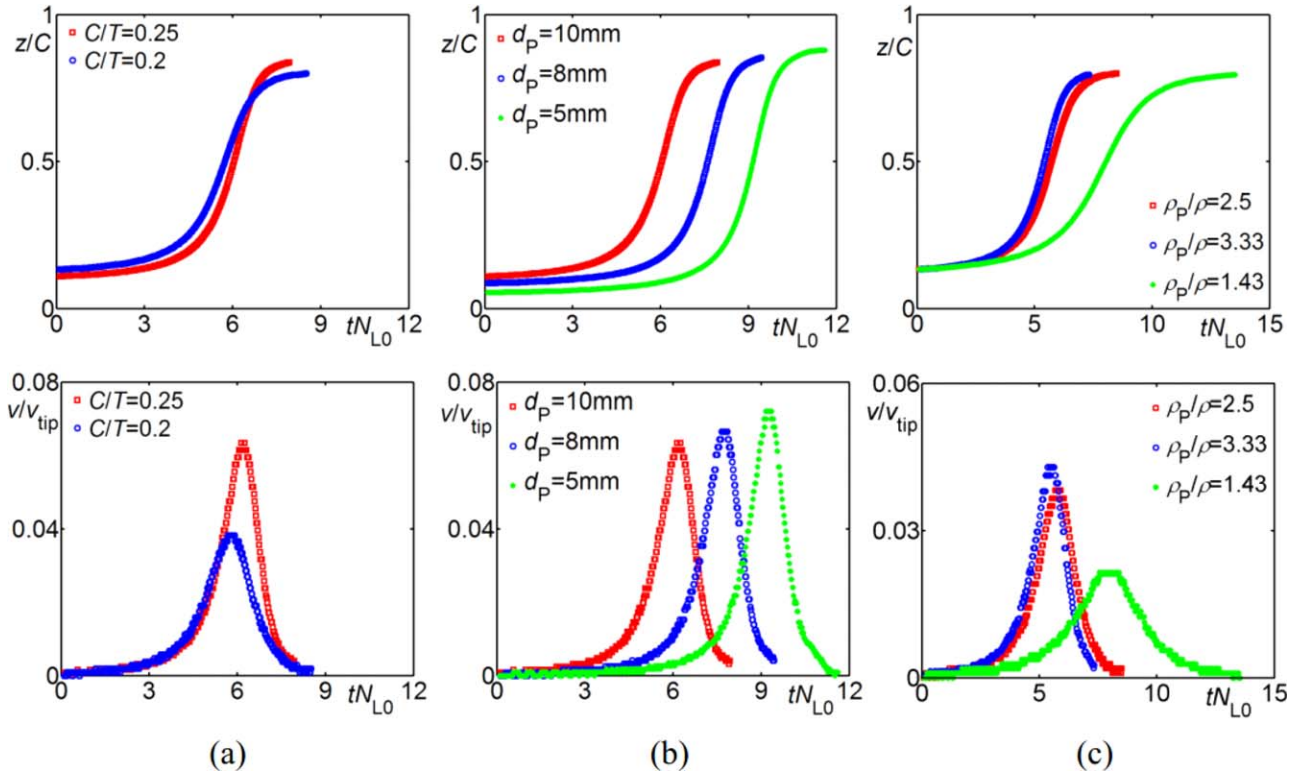

Figure 9. Time series of sphere trajectory (top) and velocity (bottom) during its rise toward the disk over the centerline of the tank.

(a) Effect of disk's off-bottom clearance (E1 vs. E4). (b) Effect of diameter of glass spheres at $C/T = 0.25$. (c) Effect of sphere density at $C/T = 0.20$ and $d_p = 10$ mm. [Color figure can be viewed in the online issue, which is available at wileyonlinelibrary.com.]

concluded that approximately $Re_{LO} \propto (\Delta\rho/\rho)^{0.7}$. This implies that the suspending force scales as $F_{susp} \propto N^{1/0.7} \approx N^{1.4}$, that is, in between viscous ($F_{susp} \propto N$) and inertial ($F_{susp} \propto N^2$) scaling. Further interpretations of the results in Table 2 will be presented in the context of the results of numerical simulations.

Visualizations of the motion of the sphere

Three subsequent stages in the particle suspension process have our particular interest: (1) rolling of the sphere over the bottom; (2) lift off and vertical rise over the center line of the tank; (3) spiraling motion underneath the disk and ejection into the tank. For two realizations of experimental case E1, the results of the quantitative visualizations are shown in Figure 7. In this case, the disk is accelerated from rest to $N_{LO} = 342$ rpm with a constant acceleration of 100 rpm/s so that N_{LO} is reached after 3.42 s. The sphere rolls over the bottom along a curved path and reaches the center of the tank after 5.54 s. It then gets lifted off, hits the lower surface of the disk, spirals around, and is eventually swirled out. The experiment shows good reproducibility in all three stages. For the vertical part of the trajectory, the velocity of the sphere has been determined by numerical differentiation (central differences) of location as a function of time (Figure 7d). This differentiation brings out some noise in the location data. Overall, however, the velocity signal is smooth. The sphere accelerates to a distinct peak velocity of about 0.065 v_{tip} before it quickly decelerates on approaching the disk.

Figure 8a shows that there is a minor, though consistent, effect of disk acceleration on the path the sphere follows while rolling over the bottom: its curvature increases with decreasing acceleration. This is likely due to the flow still developing while the sphere rolls over the bottom. The time over which the disk accelerates is a few seconds. Given the viscosity and the dimensions of the mixing tank (specifically the distance $C = 55$ or 45 mm between disk and bottom), a few seconds is also the time scale over which momentum diffuses over a distance of the order of C; over $t = 1$ s, $\sqrt{\nu t} \approx 50$ mm. The simulations (see the next subsection) confirm this time scale for flow development. For the lowest acceleration of 50 rpm/s, the flow has most time to develop during the rolling of the sphere over the bottom which leads to slightly more curvature in its path. In the remainder of the visualization experiments, the disk rotation starts by default with an acceleration of 100 rpm/s.

More dependencies on the experimental conditions appear when the rolling of the sphere over the bottom is visualized. A more strongly curved path is followed at lower disk clearance (Figure 8b); this again is for reasons of a more developed flow near the bottom for smaller C. In Figure 8c, the paths of spheres with different densities are given. The lightest sphere (made of plastic with $\rho_p/\rho = 1.43$) follows a much longer and more curved path than the other two spheres. As we will see when discussing the simulated liquid flow field (which will be done later in Figure 11), this is a Reynolds number effect and is not directly related to the sphere's density. The disk speed for lifting off the light sphere is much lower than for the other spheres and at lower Re, the radial liquid velocity component near the bottom is smaller than for higher Re giving rise to a longer trajectory of the sphere over the bottom.

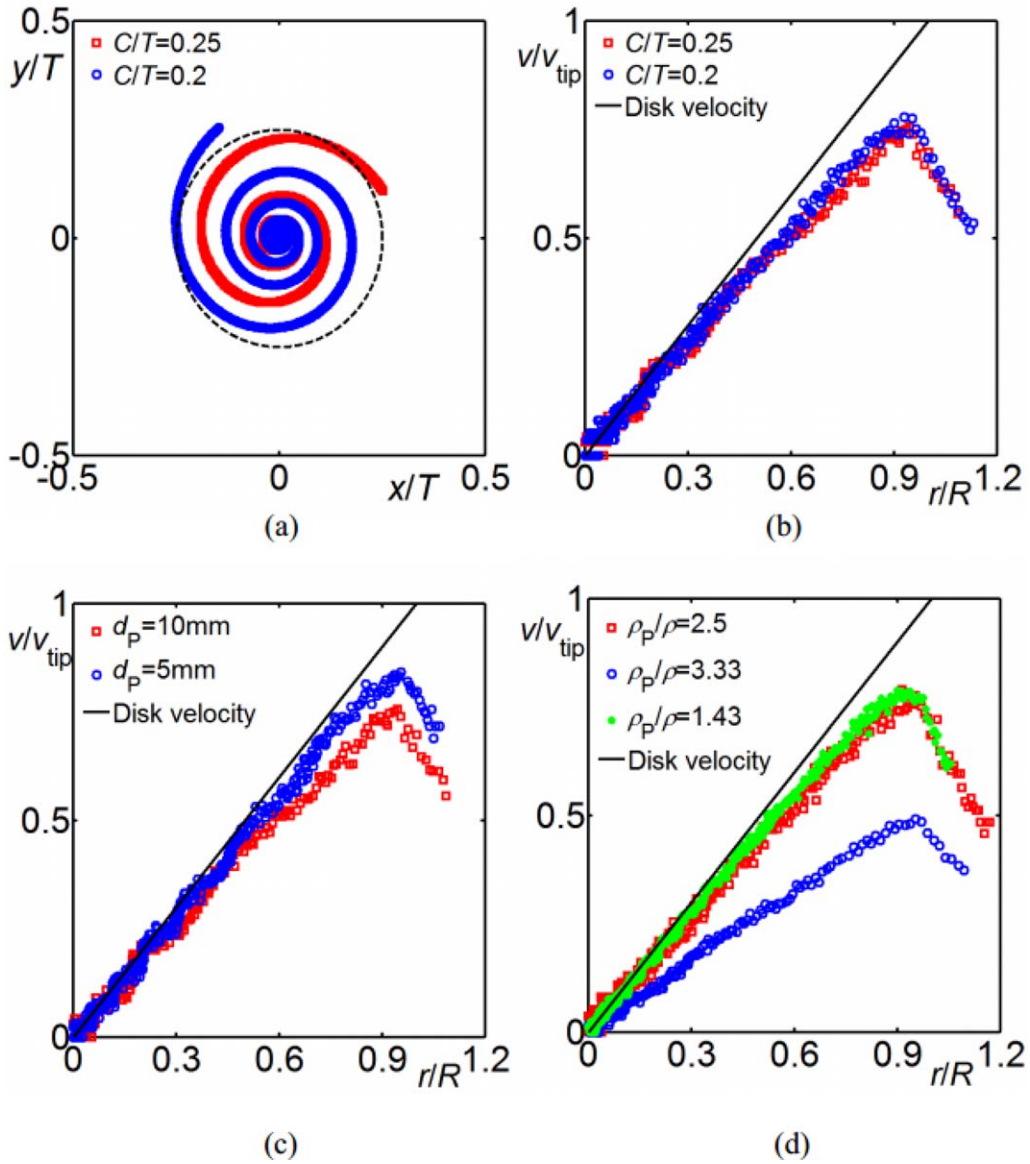

Figure 10. (a) Comparison of swirling motion of the 10 mm glass sphere under the disk for the two off-bottom clearances.

(b–d) Speed of the sphere as a function of its radial location (with $R = D/2$ the disk radius) showing limited levels of relative velocity between sphere and disk, except for the dense sphere (shown in panel [d]). Panel (b): 10 mm glass spheres; (c) $C/T = 0.25$ and glass spheres; (d) $C/T = 0.2$ and 10 mm spheres. [Color figure can be viewed in the online issue, which is available at wileyonlinelibrary.com.]

The vertical motion of the sphere is analyzed in Figure 9. The disk spins steadily with the critical lift-off rotation rate N_{LO} during the stages shown in Figure 9. As we are close to the critical condition for lift off, the initial vertical acceleration of the sphere is small. With increasing distance between the sphere and the bottom wall, net vertical hydrodynamic forces on the sphere apparently strongly increase given the strong increase in vertical acceleration which peaks when the sphere is approximately halfway the bottom and the disk. Then, the vertical velocity quickly decreases to become zero when the sphere touches the disk. With a larger disk clearance, the sphere has more room and time to accelerate and therefore, the peak vertical velocity is nearly twice as high for $C/T = 0.25$ as compared with $C/T = 0.20$ (Figure 9a). Smaller spheres get entrained more slowly by the flow: the initial, low acceleration stage is twice as long if $d_p = 5$ mm compared with 10 mm (Figure 9b). The low-density, plastic sphere behaves markedly different from the denser spheres (Figure 9c). Its rise to the disk is slower when measured in number of impeller revolutions (tN_{LO}) as we do in Figure 9c. As the lift-off disk speed of the light plastic particle is about 2.4 times less than that of the glass particle, in real time, the rise of the plastic particle takes about 3.6 times longer than of the glass particle.

At the end of its vertical path, the sphere touches the lower surface of the disk close to its center. Centrifugal forces and contact friction make that the sphere spirals away from the center while positive vertical hydrodynamic forces ensure rolling and/or slipping contact between sphere and disk surface. Figure 10 shows this spiraling motion and also shows that the speed of the sphere closely follows the local circumferential velocity of the disk surface with limited relative velocity between disk and sphere. The exception is the dense silicon nitride sphere. Its speed clearly lags that of the

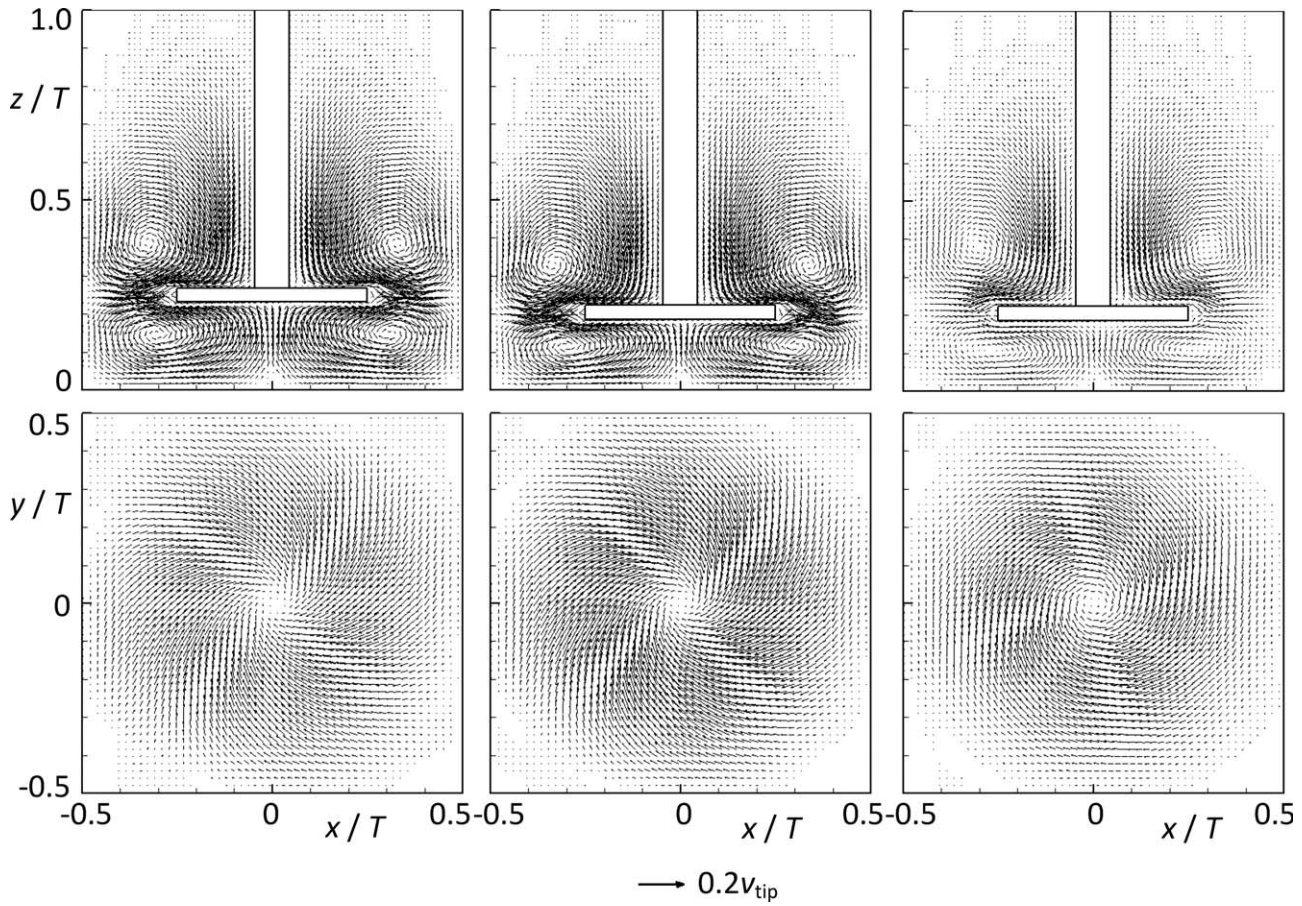

Figure 11. Impression of the simulated liquid flow (no sphere present) in terms of velocity vectors.

Flow field after 20 impeller revolutions. Resolution such that the disk diameter D spans 132 lattice spacings ($D=132\Delta$). Top row: vertical cross-sections through the center ($y = 0$); bottom row: horizontal cross-sections at $z = 0.023\ T = 5.06$ mm (which is the approxiamte vertical location of the center of a sphere with $d_p = 10$ mm lying on the bottom). Left column: $C/T = 0.25$, $Re = 31.44$; middle column: $C/T = 0.2$, $Re = 37.61$; right column: $C/T = 0.2$, $Re = 11.21$. The reference vector that indicates the tip speed applies to all six panels.

disk surface. Its high net weight likely prevents good contact with the disk.

In the next section, the experimental results will be confronted with numerical simulations. The simulations aim at resolving the liquid flow and the way the liquid interacts with the sphere. The detailed (flow) information from the simulations allows for placing some of the experimental observations in context. At the same time, the experimental data provide important validation material for the simulations.

Numerical results and comparison with experiments

Impressions of the liquid-only flow after the disk has spun sufficiently long for the flow to reach steady state are given in Figure 11. It qualitatively shows the effects of the disk clearance C and the Reynolds number. The horizontal cross-sections are taken approximately 5 mm above the bottom, that is, at the vertical location of a $d_p = 10$ mm sphere if it is supported by the bottom. Here, it shows that—as anticipated in Figure 8c—the flow at $Re = 11$ closely above the bottom has a weaker inward radial component as compared with the cases with higher Re. Note that the flow fields shown in Figure 11 are instantaneous realizations and, therefore, clearly are laminar in nature. The development to steady state is illustrated in Figure 12, where it is noted that very shortly after the end of the acceleration period of the disk the flow reaches steady state.

We now turn to simulations that include the motion of the sphere. Four of the experimental cases will be considered: E1, E2, E4, and E5, that is, the cases with 10 and 8 mm glass spheres at both disk clearances $C/T = 0.25$ and $C/T = 0.20$. The default simulation settings are that the sphere diameter is resolved by 12 lattice spacings ($d_p = 12\Delta$) and that the lubrication force model (Eq. 1) is active. The sensitivity of the results with respect to these settings will be discussed as well. As in the experiments, the simulations are started with liquid and sphere at rest, the sphere at the specified location on the bottom $\left(0.0, -0.409T, 0.5d_p\right)$, and the same acceleration of the disk as in the visualization experiments is applied. In each simulation, the Shields number is specified which—given all the other conditions of the flow system—can be directly translated in the disk's angular velocity.

In Table 3, the critical lift-off conditions as observed in the simulations are presented. For each of the experimental cases, we simulated, a lower-bound and an upper-bound critical Shields number are presented, θ_{lowb} and θ_{upb}, respectively. The value θ_{lowb} indicates the highest simulated Shields number for which the sphere did not lift off; θ_{upb} is the lowest simulated Shields number for which the sphere did lift-off.

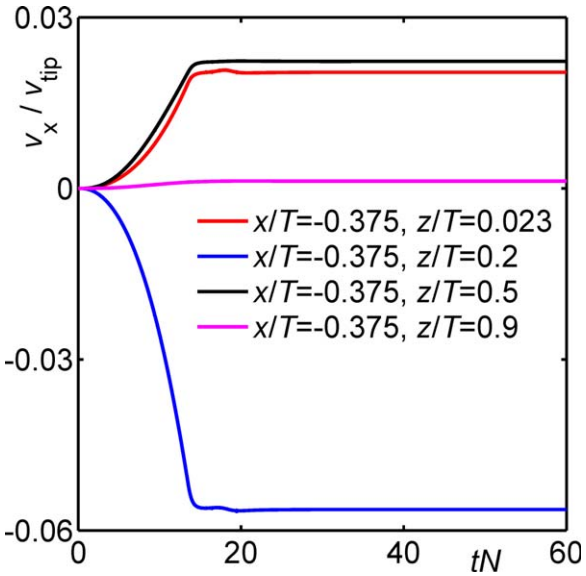

Figure 12. Time series of local flow velocities in *x*-direction in the vertical plane with $y = 0$.

In this simulation, the disk accelerates from $t = 0$ to $tN = 13.44$ with N the eventual rotation rate, that is, during the acceleration period the disk makes 6.72 revolutions. $Re = 26.04$, $C/T = 0.2$. [Color figure can be viewed in the online issue, which is available at wileyonlinelibrary.com.]

We see that for $C/T = 0.25$, the critical Shields number is overpredicted by some 10% which (given that $\theta \propto N^2$) is an overprediction of 3% of the lift-off disk speed. For $C/T = 0.20$, the agreement between simulations and experiment is better. It has further become clear that the application of the lubrication force model has no influence on the critical lift-off conditions. It is the vertical hydrodynamic force on the sphere lying on the bottom that has not yet a wall-normal velocity (and thus does not yet feel a lubrication force) that matters for lift off. The lubrication force does have a strong impact on the time scales over which the lift-off process takes place. For Case E1 at the Shields number that eventually shows lift off in the simulation, the initial rise of the sphere over a vertical distance of $0.1d_p$ can take up to 16.9 s with an active lubrication force, while the much shorter time of 4.1 s (a factor of 4 shorter) is observed without lubrication force. In that respect, the simulations with active lubrication force much better resemble the experimental observations: 16.8 and 17.9 s for the two realizations of the experiment.

In what follows the sphere's motion as simulated will be compared with the experimental data. In Figure 13, good agreement is observed between the experimental and simulated trajectories of the sphere rolling over the bottom. Also the time of travel agrees fairly well. As a measure for this, we take the time it takes for the sphere to approach the center of the bottom within a distance of $0.5d_p$.

The detailed flow information assists in understanding the precise reason for lift-off of the sphere. In Figure 14, pressure and velocity fields are shown directly around the sphere on its upward vertical path toward the disk. An important feature is the pressure minimum above the sphere when it still rests on the bottom. It is created by the swirling motion of the liquid due to the spinning disk. The negative $\partial p/\partial z$ is responsible for the initial lift off. This is consistent with the analysis of the data in Table 2 and Figure 6 that indicates that the hydrodynamic force responsible for lift off is proportional to the volume of the sphere, which is the case for a pressure-gradient force.

Above, we also noted that the suspending force scales as $F_{susp} \propto N^{1.4}$, that is, in between viscous ($F_{susp} \propto N$) and inertial ($F_{susp} \propto N^2$) scaling. It is due to the reduced pressure above the sphere when it rests on the bottom and this reduced pressure does not—due to the viscous nature of the flow—perfectly scale as N^2 but rather to some power lower than 2. This can be appreciated when one looks at Figure 11 and sees that the strength of swirl depends significantly on the disk Reynolds number (note that the velocity vectors in Figure 11 have been scaled with the tip speed of the disk and thus with N).

Shortly, after lift off, the pressure below the sphere reduces as a result of liquid being drawn in the widening gap between bottom and sphere. As can be seen in the second frame of Figure 14 (at $tN = 3$), still $\partial p/\partial z < 0$. At this stage, also the upward vertical liquid flow assists in lifting the sphere further. On approach of the spinning disk, the pressure above the sphere increases as liquid needs to be squeezed out of the gap between disk and sphere (as in the final panel of Figure 14).

In Figure 15, the vertical part of the sphere's trajectory is considered and experimental and computational results compared. Most importantly, these results have been used to assess the effect of spatial resolution of the simulations. The vertical location and velocity as a function of time for simulations at or close to the upper bound Shields numbers θ_{upb} (Table 3) are compared with experiments at θ_{LO}. The agreement is generally good. Grid refinement (to $d_p = 14\Delta$) and coarsening (down to $d_p = 8\Delta$) have marginal effect on the results (Figure 15c).

Finally, the spiraling motion underneath the disk has been investigated. It is recovered by the simulations. A precise match between measured and simulated paths was not observed (Figure 16). One reason is due to the strong sensitivity of the spiraling path with respect to the point of initial contact between sphere and disk. Another reason might be that the lubrication model was not incorporated for the sphere approaching the lower surface of the disk. As a global characteristic of the motion underneath the disk, the time the sphere is in contact with the disk was taken. This time is typically less than 1 s. As indicated in Figure 16, these times are well reproduced by the simulations.

Table 3. Lift-Off Shields Numbers; Experiments and Simulations

Case	Particle	$\rho_p/\rho(-)$	$C/T(-)$	d_p (mm)	$v\rho$ (Pa·s)	Ar $(-)$	θ_{LO}exp. $(-)$	θ_{lowb}sim $(-)$	θ_{upb}sim. $(-)$
E1	Glass	2.50	0.25	10	2.143	3.07	2.66	2.66	2.92
E2				8	2.137	1.58	3.02	3.02	3.32
E4			0.2	10	2.149	3.06	1.83	1.65	1.83
E5				8	2.143	1.57	2.13	1.92	2.13

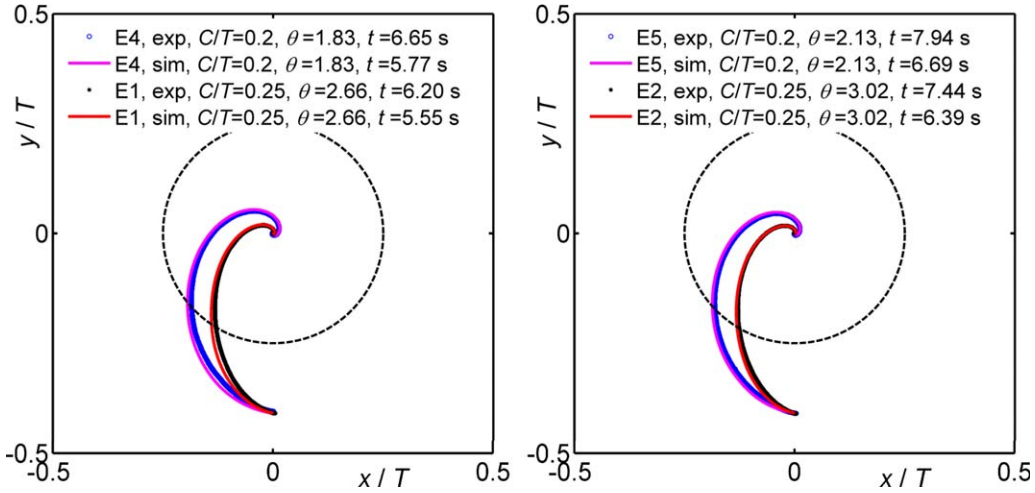

Figure 13. Rolling of glass sphere on bottom, simulation and experiment. Left: $d_p = 10$ mm; right: $d_p = 8$ mm.

The time listed is the time it takes for the sphere to move from the starting location on the bottom $(0.0, -0.409T, 0.5d_p)$ to a location within a distance of $0.5d_p$ from the center of the bottom. [Color figure can be viewed in the online issue, which is available at wileyonlinelibrary.com.]

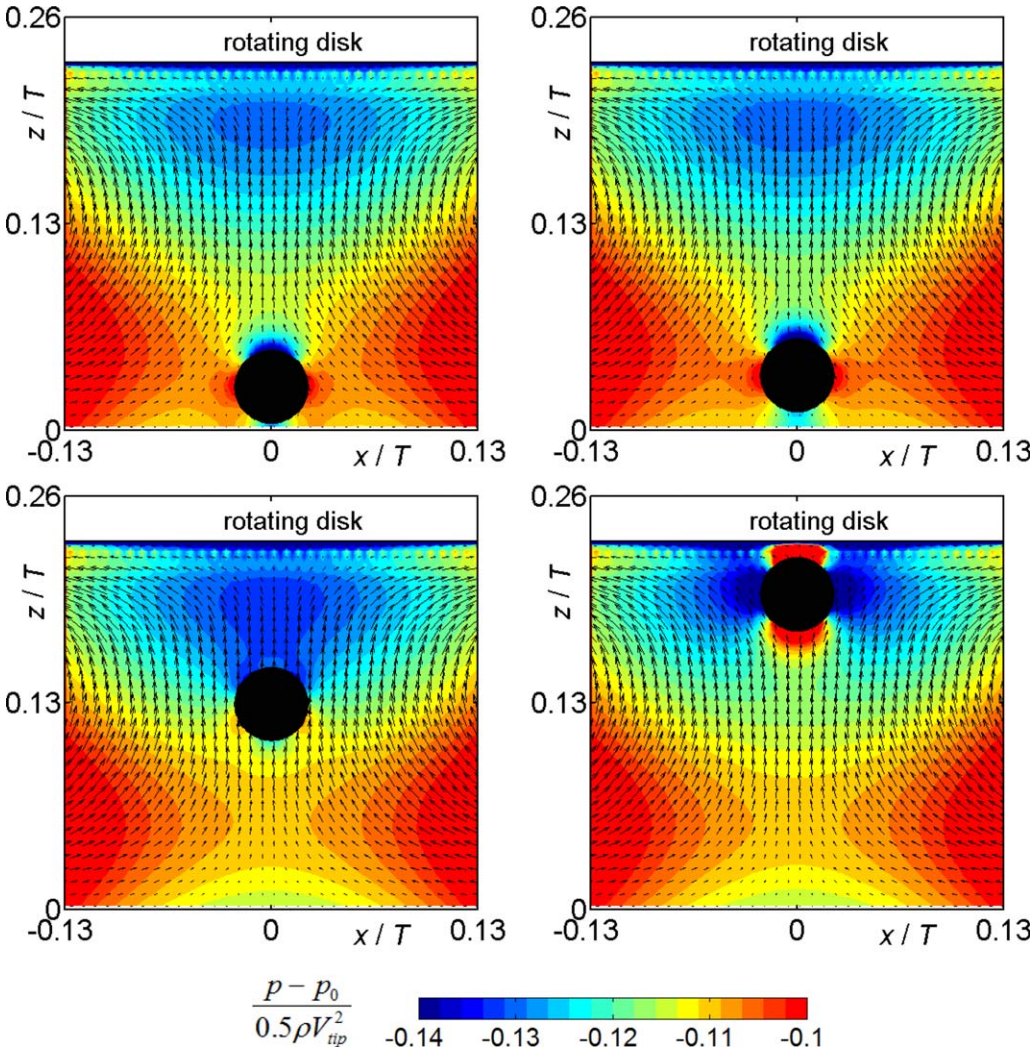

Figure 14. Normalized flow field and pressure distribution during the lift off of a 10 mm glass particle (Case E1, $C/T = 0.25$, $d_p = 12\Delta$, $\theta = 2.92$).

Lubrication force was included in this simulation. The dimensionless times tN for the top left, top right, bottom left, and bottom right panels are 0, 3, 6, and 7, respectively. [Color figure can be viewed in the online issue, which is available at wileyonlinelibrary.com.]

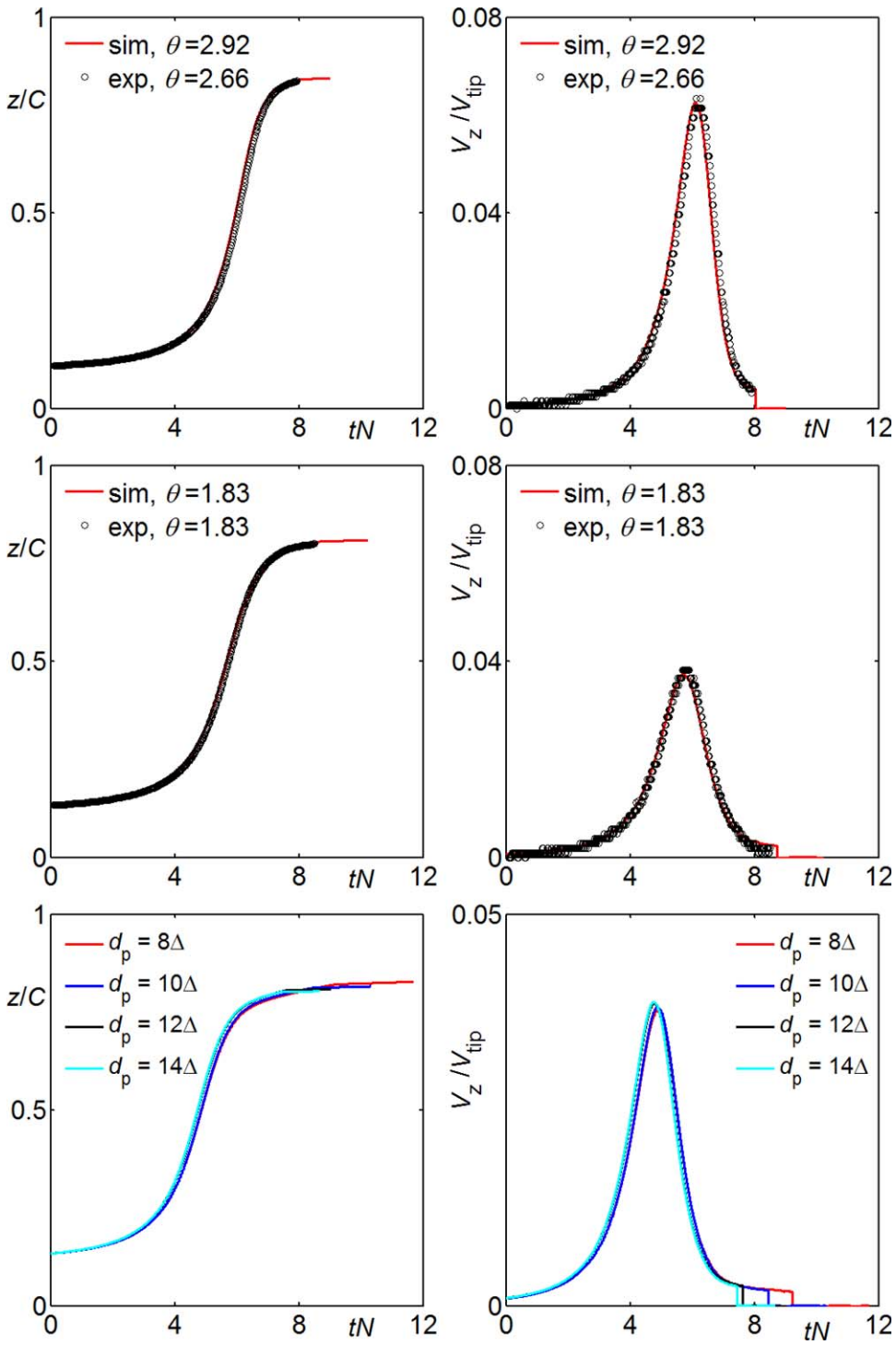

Figure 15. Particle axial position vs. dimensionless time (left column) and particle vertical velocity vs. dimensionless time (right column).

Top row: Case E1, $C/T = 0.25$, $d_p = 12\Delta$; middle row: Case E4, $C/T = 0.2$, $d_p = 12\Delta$; bottom row: Case E4, $C/T = 0.2$, $\theta = 2$. Lubrication force was included in all simulations. [Color figure can be viewed in the online issue, which is available at wileyonlinelibrary.com.]

Conclusions and Future Work

In this article, we have generated an experimental data set on critical conditions for a single sphere being suspended by a laminar liquid flow that resembles the flow in a mixing tank: a rotating disk generates a swirling flow in a square container. The flow systems and scenarios for lift off of the sphere have been described in detail so that the cases discussed allow for the execution of numerical simulations that very closely match experimental conditions. This article also describes the application of one of such simulation approaches.

It is concluded from parameter variations in the experiment that the vertical force responsible for lift off of the sphere is approximately proportional to the sphere's volume. Based on observations from the simulations, this force has

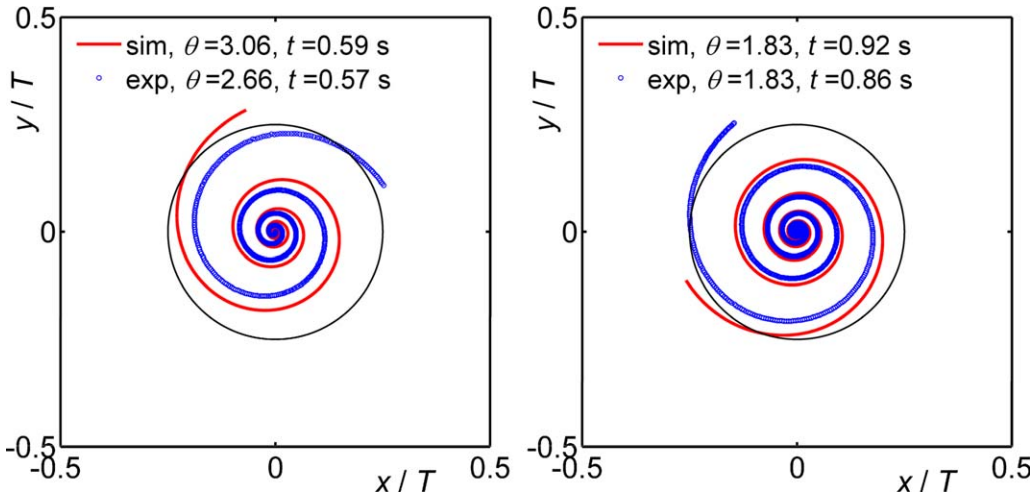

Figure 16. Spiraling motion of a glass sphere with $d_p = 10$ mm under the disk; simulation and experiment.

Left: Case E1, $C/T = 0.25$; right: Case E4, $C/T = 0.2$. The time listed is the time it takes for the sphere going from a radial distance $0.5d_p$ from the center of the disk to the edge of the disk. [Color figure can be viewed in the online issue, which is available at wileyonlinelibrary.com.]

been identified as a pressure-gradient force. The scaling of the suspending force with the strength of the flow—that has been quantified by the rotational speed of the disk N—is such that $F_{susp} \propto N^{1.4}$ which is intermediate between viscous and inertial scaling.

In addition to identifying critical lift-off conditions, particle trajectories and velocities have been measured by high-speed imaging and quantitative image analysis. These trajectories have been compared with the outcomes of our numerical approach based on the LB method with an immersed boundary approach to imposing no-slip conditions at moving surfaces (the spinning disk and the moving and rotating sphere). Good agreement of simulation results with experimental data in the various stages of particle motion has been observed. A grid-refinement study shows that the simulations are sufficiently resolved. In terms of the inertial Shields number $\theta \equiv \frac{\rho N^2 D^2}{g\Delta\rho d_p}$, the critical lift-off conditions as simulated are within 10% of the critical conditions as measured. It has also been found that inclusion of the lubrication force in the simulations (to compensate for lack of resolution if solid surfaces are within one lattice spacing) has no influence on the critical lift-off conditions. It does have an impact, however, on the time scales over which lift off takes place.

It needs to be emphasized that in practical (chemical engineering) applications, particle entrainment mechanisms are more complex and rich than the ones described in this article. In future research, we will be systematically adding complexity to the "base-case" as described here. By adding more spheres to the same (disk-in-square-tank) mixing configuration, we will study how collective behavior assists suspending processes. As is known from sheared granular beds,[38] rolling of spheres over one another helps in exposing them to liquid flow and thus enhances entrainment. Admittedly, the behavior of a swarm of suspended particles will be more complex than a simple extrapolation of the behavior of few particles. A more complex impeller (e.g., a down-pumping pitched-blade turbine or a Rushton turbine) makes the liquid flow unsteady (due to blade-passage effects) of which it will be interesting to study how these fluctuations will affect single and multiple sphere entrainment. Introducing fluctuations will also be a step toward studying the effects of turbulence on solids suspension processes in mixing tanks. As is known from swirling flows, the Ekman vortex enhances turbulence levels and the entrainments of particles into the liquid.[39,40]

Acknowledgment

The authors gratefully acknowledge the financial support from the National Natural Science Foundation of China (No. 21376016).

Literature Cited

1. Zwietering ThN. Suspending of solid particles in liquid by agitators. *Chem Eng Sci*. 1958;8:244–253.
2. Nienow AW. Suspension of solid particles in turbine agitated baffled vessels. *Chem Eng Sci*. 1968;23:1453–1459.
3. Baldi G, Conti R, Alaria E. Complete suspension of particles in mechanically agitated vessels. *Chem Eng Sci*. 1978;33:21–25.
4. Davies JT. Particle suspension and mass transfer rates in agitated vessels. *Chem Eng Process*. 1986;20:175–181.
5. Montante G, Micale G, Magelli F, Brucato A. Experiments and CFD predictions of solid particle distribution in a vessel agitated with four pitched blade turbines. *Chem Eng Res Des*. 2001;79:1005–1010.
6. Montante G, Magelli F. Mixed solids distribution in stirred vessels: experiments and computational fluid dynamics simulations. *Ind Eng Chem Res*. 2007;46:2885–2891.
7. Ayranci I, Kresta SM. Design rules for suspending concentrated mixtures of solids in stirred tanks. *Chem Eng Res Des*. 2011;89:1961–1971.
8. Bong CHJ, Lau TL, Ab Ghani A. Verification of equations for incipient motion studies for a rigid rectangular channel. *Water Sci Technol*. 2013;67:395–403.
9. Rabinovich E, Kalman H. Threshold velocities of particle-fluid flows in horizontal pipes and ducts: literature review. *Rev Chem Eng*. 2011;27:215–239.
10. Soepyan FB, Cremaschi S, Sarica C, Subramani HJ, Kouba GE. Solids transport models comparison and fine-tuning for horizontal, low concentration flow in single-phase carrier fluid. *AIChE J*. 2014;60:76–122.
11. O'Neill ME. A sphere in contact with a plane wall in a slow linear shear flow. *Chem Eng Sci*. 1968;23:1293–1298.
12. Leighton D, Acrivos A. The lift on a small sphere touching a plane in the presence of a simple shear flow. *J Appl Math Phys*. 1985;36:174–178.
13. Krishnan GP, Leighton DT. Inertial lift on a moving sphere in contact with a plane in a shear flow. *Phys Fluids*. 1995;7:2538–2545.

14. Patankar NA, Huang PY, Ko T, Joseph DD. Lift-off of a single particle in Newtonian and viscoelastic fluids by direct numerical simulation. *J Fluid Mech.* 2001;438:67–100.
15. Zeng L, Balachandar S, Fischer P. Wall-induced forces on a rigid sphere at finite Reynolds number. *J Fluid Mech.* 2005;536:1–25.
16. Zeng L, Najjar F, Balachandar S, Fischer P. Forces on a finite-sized particle located close to a wall in a linear shear flow. *Phys Fluids.* 2009;21:033302.
17. Segre G, Silberberg A. Behaviour of macroscopic rigid spheres in Poiseuille flow. Part 2: experimental results and interpretation. *J Fluid Mech.* 1962;14:136–157.
18. Van der Hoef MA, Beetstra R, Kuipers JAM. Lattice-Boltzmann simulations of low-Reynolds-number flow past mono- and bidisperse arrays of spheres: results for the permeability and drag force. *J Fluid Mech.* 2005;528:233–254.
19. Charru F, Larrieu E, Dupont J-B, Zenit F. Motion of a particle near a rough wall in a viscous shear flow. *J Fluid Mech.* 2007;570:431–453.
20. Agudo JR, Dasilva S, Wierschem A. How do neighbors affect incipient particle motion in laminar shear flow. *Phys Fluids.* 2014;26:053303.
21. Derksen JJ. Highly resolved simulations of solids suspension in a small mixing tank. *AIChE J*. 2012;58:3266–3278.
22. Canny J. A computational approach for edge detection. *IEEE Trans Pattern Anal*. 1986;8:679–698.
23. Hough PVC. Method and means for recognizing complex patterns. US Patent 3,069,654, 1962.
24. Chen S, Doolen GD. Lattice Boltzmann method for fluid flows. *Annu Rev Fluid Mech.* 1989;30:329–364.
25. Succi S. *The Lattice Boltzmann Equation for Fluid Dynamics and Beyond*. Oxford: Clarendon Press, 2001.
26. Somers JA. Direct simulation of fluid flow with cellular automata and the lattice-Boltzmann equation. *Appl Sci Res.* 1993;51:127–133.
27. Eggels JGM, Somers JA. Numerical simulation of free convective flow using the lattice-Boltzmann scheme. *Int J Heat Fluid Flow*. 1995;16:357–364.
28. Derksen J, Van den Akker HEA. Large eddy simulations on the flow driven by a Rushton turbine. *AIChE J*. 1999;45:209–221.
29. Ten Cate A, Nieuwstad CH, Derksen JJ, Van den Akker HEA. Particle imaging velocimetry experiments and lattice-Boltzmann simulations on a single sphere settling under gravity. *Phys Fluids*. 2002;14:4012–4025.
30. Feng ZG, Michaelides E. Robust treatment of no-slip boundary condition and velocity updating for the lattice-Boltzmann simulation of particulate flows. *Comput Fluids*. 2009;38:370–381.
31. Ladd AJC. Numerical simulations of particulate suspensions via a discretized Boltzmann equation. Part 1: theoretical foundation. *J Fluid Mech.* 1994;271:285–309.
32. Sangani AS, Acrivos A. Slow flow through a periodic array of spheres. *Int J Multiphase Flow*. 1982;8:343–360.
33. Yamamoto Y, Potthoff M, Tanaka T, Kajishima T, Tsuji Y. Large-eddy simulation of turbulent gas-particle flow in a vertical channel: effect of considering inter-particle collisions. *J Fluid Mech.* 2001;442:303–334.
34. Derksen JJ, Sundaresan S. Direct numerical simulations of dense suspensions: wave instabilities in liquid-fluidized beds. *J Fluid Mech*. 2007;587:303–336.
35. Derksen JJ. Simulations of granular bed erosion due to laminar shear flow near the critical Shields number. *Phys Fluids*. 2011;23:113303.
36. Kim S, Karrila SJ. *Microhydrodynamics: Principles and Selected Applications*. Boston: Butterworth-Heinemann, 1991.
37. Nguyen N-Q, Ladd AJC. Lubrication corrections for lattice-Boltzmann simulations of particle suspensions. *Phys Rev E*. 2002;66:046708.
38. Charru F, Mouilleron H, Eiff O. Erosion and deposition of particles on a bed sheared by a viscous flow. *J Fluid Mech*. 2004;519:55–80.
39. Volk R, Calzavarini E, Leveque E, Pinton JF. Dynamics of inertial particles in a turbulent von Karman flow. *J Fluid Mech.* 2011;668:223–235.
40. Lavezzo V, Verzicco R, Soldati A. Ekman pumping and intermittent particle resuspension in a stirred tank reactor. *Chem Eng Res Des.* 2009;87:557–564.

Manuscript received Nov. 20, 2014, and revision received Jan. 2, 2015.